Ultrastrong and ductile NiTi-based composite with large recoverable strain mediated by a compositionally complex phase

Jiayi Geng[1,4], Yunzhu Shi[1,*], Pere Barriobero-Vila[2,3], Meiyuan Jiao[5], Yihuan Cao[5], Yu Tang[6], Jingzhi He[6], Chao Ma[1], Yan Ma[7], Zhifeng Lei[1,*], Zhaoping Lu[5,*]

[1]College of Materials Science and Engineering, Hunan University, Changsha, 410082, China

[2]Department of Materials Science and Engineering, Technical University of Catalonia (UPC), Barcelona 08019, Spain

[3]CIM, Technical University of Catalonia (UPC), Barcelona 08028, Spain

[4]State Key Laboratory of High-Performance Ceramics and Superfine Microstructure, Shanghai Institute of Ceramics, Chinese Academy of Sciences, Shanghai, 200050, China

[5]Beijing Advanced Innovation Center for Materials Genome Engineering, State Key Laboratory for Advanced Metals and Materials, University of Science and Technology Beijing, Beijing 100083, China

[6]College of Aerospace Science and Engineering, National University of Defense Technology, Changsha 410073, China

[7]Max-Planck-Institut für Eisenforschung, Max-Planck-Straße 1, 40237 Düsseldorf, Germany

[*]Corresponding authors. Email: yzshi@hnu.edu.cn (Yunzhu Shi); zflei@hnu.edu.cn (Zhifeng Lei); luzp@ustb.edu.cn (Zhaoping Lu).

Abstract

NiTi-based composites possess great potential for concurrently improving both mechanical and functional properties. However, relying on traditional alloy design principles limits the design space and greatly hinders the advancement of high-performance NiTi-based composites. The concept of high-entropy alloys has expanded the compositional landscape, unveiling unique structural characteristics for alloy design and providing new prospects for addressing these limitations. Here, we report a compositionally complex NiTi-based composite that exhibits exceptional strength and ductility, along with remarkable recoverable strain. The composite, $Ni_{40}Ti_{40}(NbMoTaW)_{20}$ (at.%), comprises a 78.0% B2 NiTi matrix, a 19.2% Nb-Mo-Ta-W-Ti-Ni compositionally complex body-centered cubic (BCC) phase, and a small amount of Ti_2Ni. Notably, this composite achieves a compressive strength of 3274 MPa, a fracture strain of 44.2%, and a recoverable strain of 7.3%. These outstanding mechanical properties arose from the interplay between the compositionally complex phase and lattice strain matching facilitated by phase transformations. The substantial recoverable strain was obtained through the reversible B2⇌R⇌B19' phase transition. This work not only innovates a new category of high-performance NiTi-based composites but also extends the applicability of the high-entropy concept.

Keywords: NiTi-based composites; High-entropy alloys; Mechanical properties; Recoverable strain; Phase transformation.

Introduction

Shape memory alloys fall within the category of smart materials, owing to their remarkable capability to undergo substantial reversible phase transformations that define their functional properties[1–3]. NiTi alloys with a simple CsCl (B2) structure lead in shape memory alloys due to their outstanding attributes: exceptional shape memory effect, pseudoelasticity, strong corrosion resistance, biocompatibility, and good processability[4–6]. To cope with the increasingly challenging and intricate service environment, expanding industrail application of NiTi alloys primarily involves improving their mechanical properties and functional capabilities. To meet this demand, NiTi-based composites, such as NiTi-metal and NiTi-intermetallic compound composites, have become widely adopted solutions. Examples of these composites include NiTi-Nb[1], NiTi-W[7], NiTi-V[8], NiTi-NbTi[9], NiTi-Ti_3Sn[5], NiTi-Ti_5Si_3[10] and NiTi-Nb_3Sn[11]. Of particular note is the NiTi-Nb composite, which has a substantial quasi-linear elastic strain of over 6% and an impressive yield strength of 1.65 GPa[1]. However, conventional design principles restrict the composition range of NiTi-based metallic composites, hindering their further development and performance optimization. Moreover, traditional NiTi-based composites are usually soft due to occurrence of martensitic transformation. Intermetallic compounds, characterized by their rigidity and brittleness, hinder efforts to improve ductility and recoverable strain. Therefore, developing innovative NiTi-based composites is imperative to tackle these challenges.

The alloy design concept of high-entropy alloys (HEAs) composed of multiple principal components is a promising solution to address these challenges. The strong configuration entropy effect inherent in HEAs allows for a considerably wide range of compositions in alloy design[12–14]. This compositional diversity endows HEAs with great potential to integrate various performance attributes[15]. Moreover, the variations in atomic size and chemistry among the multiple constituents lead to large lattice distortion. This phenomenon serves to impede dislocation movement, thereby

substantially enhancing the strength of HEAs[16–20]. In addition, the complex short-range ordering within these solid solutions enriches their plastic deformation mechanisms, thereby improving their ductility[21–26]. Therefore, utilizing the concept of HEAs reveals captivating opportunities for advancing NiTi-based composites.

Stimulated by the field of HEAs, here, we developed a NiTi-based composite, achieving remarkable strength and ductility, coupled with a significant recoverable strain. The $Ni_{40}Ti_{40}(NbMoTaW)_{20}$ (at.%) composite exhibits a compressive strength of 3274 MPa, a fracture strain of 44.2%, and a recoverable strain of 7.3%. This composite comprises an Nb-Mo-Ta-W-Ti-Ni compositionally complex body-centered cubic (BCC) phase (19.2% area fraction) embedded in the B2 NiTi matrix (78.0% area fraction), along with a dispersion of a small amount of Ti_2Ni phase. The compositionally complex phase and the phase transformation-assisted lattice strain matching contribute to the exceptional mechanical properties. The large recoverable strain originates from the reversible B2⇌R⇌B19' phase transformation. The current findings not only introduce a new class of NiTi-based composites for engineering applications, but also offer insights into the design of innovative multifunctional metallic materials using the HEA concept.

Results

Mechanical and superelastic properties

Figure 1a illustrates the compressive engineering and true stress-strain curves of the $Ni_{40}Ti_{40}(NbMoTaW)_{20}$ composite, revealing a prominent double-yielding phenomenon. Stress-induced martensitic transformation of the B2 NiTi phase within the composite contributes to the first yielding[27]. The first yield stress σ_{FY} and strain ε_{FY} are 469±24 MPa and 2.87%±0.16%, respectively, whilest the second yield stress σ_{SY} and strain ε_{SY} are 1089±30 MPa and 11.34±0.55%, respectively. The ultimate strength σ_{US} and fracture strain ε_{FS} are significantly increased to 3274±56 MPa and 44.2%±0.2%, respectively. **Supplementary Figure 1** presents the fracture morphology of the composite, showing pronounced ductile tearing and a large number of dimples in $Ni_{40}Ti_{40}(NbMoTaW)_{20}$, indicative of its superior ductility. **Figure 1b** shows a plot of the ultimate strength against fracture strain for the current $Ni_{40}Ti_{40}(NbMoTaW)_{20}$, and previously reported NiTi-based alloys and composites. For comparison, compressive mechanical properties of the $Ni_{40}Ti_{40}Nb_{20}$ composite were also examined (**Supplementary Figure 2**). The $Ni_{40}Ti_{40}(NbMoTaW)_{20}$ composite exhibits high strength and large ductility. In addition, the composite features a low Young's modulus of 17.9±0.9 GPa, enabling significant elastic strain under low stress conditions and potentially enhancing its superelastic performance.

Figure 1c depicts the compressive cyclic stress-strain curve of $Ni_{40}Ti_{40}(NbMoTaW)_{20}$. Notably, during cyclic loading, the ultimate strength and fracture strain of the composite are consistent with those under continuous loading (**Figure 1a**). By analyzing the cyclic stress-strain curve, we calculated the superelastic strain ε_{SE} and recoverable strain ε_{RS} of the composite (**Supplementary Figure 3**). Initially, the superelastic strain ε_{SE}, induced by the reversed martensite to austenite phase transformation, increases during the first three cycles (ε<9%) and stabilizes at approximately 1.5% (see the lower part of **Supplementary Figure 3b**). In contrast, the

recoverable strain ε_{RS} of the composite increases with cyclic loading. The recoverable strain climbs from 2.1% to 7.3% under cyclic loading (see the upper part of **S3b**). Thus, $Ni_{40}Ti_{40}(NbMoTaW)_{20}$ exhibits not only superb mechanical properties but also attractive superelastic characteristics. **Figure 1d** compares the superelastic properties of $Ni_{40}Ti_{40}(NbMoTaW)_{20}$ with the $Ni_{40}Ti_{40}Nb_{20}$ composite (**Supplementary Figure 4**) and other NiTi-based alloys/composites[28,29]. As shown, $Ni_{40}Ti_{40}(NbMoTaW)_{20}$ shows a maximum recoverable strain comparable to NiTi-Nb and NiTi-Ag composites, underscoring its superior superelastic features.

Microstructure characterization

To unveil the intrinsic mechanisms governing the mechanical and superelastic properties of this material, we meticulously examined its phase constitutions. **Figure 2a** displays the high-energy X-ray diffraction (XRD) pattern of $Ni_{40}Ti_{40}(NbMoTaW)_{20}$. The composite primarily consists of B2 and BCC phases, accompanied by a limited quantity of Ti_2Ni and R phases. **Figure 2b** captures a scanning electron microscope (SEM) micrograph of the $Ni_{40}Ti_{40}(NbMoTaW)_{20}$ composite, unveiling a microstructure characterized by large white particles dispersed throughout the matrix. After careful examination, the matrix and white strips form a mesh-like eutectic structure, with a small number of black strips located at the junctions of the mesh-like white strips (**Figure 2c**). The corresponding energy-dispersive X-ray spectroscopy (EDS) results reveal that Ni and Ti elements are enriched in the matrix, Nb, Mo, Ta, and W elements are enriched in the large white particles and white strips, and Ni and Ti elements are enriched in the black strips (**Supplementary Figure 5**). The detailed compositions for each phase are provided in **Table S1**. In the matrix, the atomic ratio of Ni and Ti elements is close to 1:1, while in the black strips, the ratio tends to be 1:2. Combining the high-energy XRD and SEM results, it was found that the matrix corresponds to the B2 NiTi phase, the black strips is the Ti_2Ni phase, and the white particles and strips are the BCC phase. Specifically, for the BCC phase in $Ni_{40}Ti_{40}(NbMoTaW)_{20}$, the concentration of Ni, Ti, Nb, Mo, Ta and W were measured to be 10.05±2.50 at.%,

19.95±3.84 at.%, 13.96±1.77 at.%, 13.51±0.93 at.%, 18.23±1.36 at.% and 24.29±6.82 at.%, respectively. The BCC phase exhibits an ideal configurational mixing entropy of approximately 14.56 $J \cdot mol^{-1} \cdot K^{-1}$, well within the range established for HEAs by Yeh et al[30]. Moreover, the area fractions of the B2, BCC, and Ti_2Ni phases were determined to be 78.0%±4.1%, 19.2%±5.3%, and 2.8%±1.6%, respectively. Therefore, we can classify the current BCC phase as a compositionally complex phase.

To delve into the atomic-scale microstructure features of $Ni_{40}Ti_{40}(NbMoTaW)_{20}$, we utilized transmission electron microscopy (TEM). **Figure 2d** shows a representative bright-field TEM image. The selected area electron diffraction (SAED) pattern (**Figures. 2d1-d3)** clearly identifies the matrix as B2, white strips as BCC, and black strips as Ti_2Ni. The B2 and BCC structures were further affirmed through a high-resolution TEM image and the corresponding fast Fourier transformation (FFT) image (**Supplementary Figure 6**). Both distinctly illustrate the ordered atomic arrangement of B2 versus the disordered atomic arrangement of BCC. The corresponding TEM-EDS mapping analysis further demonstrates the enrichment of Nb, Mo, Ta, and W elements in the BCC phase, while Ni and Ti elements dominate the composition of the B2 matrix and Ti_2Ni phase (**Figure 2d**). Remarkably, the Ni enrichment in the Ti_2Ni phase is lower than that in the B2 matrix, whereas the Ti enrichment follows an opposite trend. The Ti_2Ni strips exhibit a tendency to connect the BCC phase, forming a continuous mesh-like structure. A similar structure, arising from the partial substitution of Ti atoms by Nb atoms in the B2 phase, has also been observed in NiTi-Nb composites. This phenomenon leads to the accumulation of expelled Ti atoms at grain boundaries, thus resulting in the formation of the Ti_2Ni phase[31]. It is worth noting that other refractory elements may have similar effects.

Transformation behavior

To comprehend the phase transformation mechanisms in the present $Ni_{40}Ti_{40}(NbMoTaW)_{20}$ composite, we conducted differential scanning calorimetry

(DSC) measurement (**Figure 3a**). In the heating and cooling cycle, the material manifests two exothermic peaks and two endothermic peaks. Microstructure analysis reveals the predominant presence of the B2 NiTi and BCC phases within the composite. Specifically, when doped with additional elements, the B2 NiTi phase typically experiences a two-step phase transition B2⇌R⇌B19'. This dual transformation is characterized by two exothermic peaks and two endothermic peaks[32]. Thus, it can be deduced that the $Ni_{40}Ti_{40}(NbMoTaW)_{20}$ composite undergoes a two-step B2⇌R⇌B19' phase transformation during both the cooling and heating cycles. In this case, both the R and B19' phases undergo diffusionless transformations characterized by minimal displacements. The R phase takes the form of a rhombic structure resulting from the elongation of B2 along the [111] direction, while B19' adopts a monoclinic structure formed by the displacement of a pair of orthogonal (110) crystal faces in B2 by a certain distance[6,33,34]. The specific reversible transformation process can be described as follows: $(\bar{1}\bar{1}1)_{B2} \rightleftharpoons (100)_R$; $(\bar{1}21)_{B2} \rightleftharpoons (010)_R$; $(2\bar{1}1)_{B2} \rightleftharpoons (001)_R$; $(111)_R \rightleftharpoons (100)_{B19'}$; $(\bar{2}11)_R \rightleftharpoons (010)_{B19'}$; and $(0\bar{1}1)_R \rightleftharpoons (001)_{B19'}$ (**Figure 3b**). The occurrence of this two-step transition within the B2 phase in NiTi-based composites is associated with factors such as the introduction of a third element and the ratio of Ni to Ti elements[33,35]. This implies that the inclusion of refractory elements may facilitate the transition from B2 to the R phase. The B2→R transformation start temperature (R_s) and the R→B19' martensitic transformation start temperature (M_s) are measured at 35.4°C and -85.7°C, respectively. The R_s value exceeds room temperature, suggesting the likely presence of the R phase in the $Ni_{40}Ti_{40}(NbMoTaW)_{20}$ composite. This aligns with the high-energy XRD result (**Figure 2a**). Also, the low M_s implies a significant difference in chemical potential between B19' and B2 in $Ni_{40}Ti_{40}(NbMoTaW)_{20}$, potentially yielding a substantial driving force for the reverse transition from B19' to B2. Moreover, the B19'→R transition finish temperature (R'_f) and the R→B2 austenitic transformation finish temperature (A_f) are measured at -46.5°C and 71.7°C, respectively. The low R'_f suggests a thermodynamically favored transition from the B19' phase to the R phase.

Deformation mechanisms

To unravel the deformation mechanism exhibited by $Ni_{40}Ti_{40}(NbMoTaW)_{20}$ composite under both continuous and cyclic loading, we conducted *in-situ* synchrotron XRD experiments. **Figure 4a** depicts the *in-situ* synchrotron XRD measurement during continuous loading, revealing a four-stage deformation process. In stage I (macro-strain ε=0-1.8%), we observe the presence of only the BCC and B2 phases. Notably, their peak positions exhibit subtle leftward shifts, while their peak widths remain largely unaltered. Consequently, this initial stage is primarily characterized by the elastic deformation of the BCC and B2 phases. Moving on to stage II (ε=1.8%-2.6%), we observe that the peak positions of the BCC phase continue to shift slightly leftward, indicating that the BCC phase remains in the elastic deformation period. Concurrently, the transition from the B2 phase to the R phase commences, and with further deformation, the emergence of the B19' phase follows suit, while the retained B2 phase continues its elastic deformation. As we transition into stage III (ε=2.6%-8.6%), the B2 phase undergoes a significant transformation into the R phase and subsequently into the B19' phase. Thus, during this stage, the deformation of the composite is primarily driven by the B2→R→B19' phase transformation. Stage IV (ε>8.6%) witnesses the composite mainly comprising the BCC and B19' phases. Though the peak positions of both phases display minimal changes, the peak widths progressively increase with deformation, signifying that this stage is primarily characterized by the plastic deformation of both phases. **Figure 4b** illustrates the lattice strain of the BCC and B2 phases during continuous loading. In the elastic strain regime (stage I and II, ε=0-2.6%), the BCC phase demonstrates a maximum lattice strain of 0.45%, while the B2 phase undergoes elastic deformation at macro-strain ε of less than 2.6%. Remarkably, the BCC phase exhibits a substantial elastic strain (ε=2.7%) during loading, closely resembling the onset strain for the B19' transition (stage II, ε=1.8%-2.6%) (**Figure 4c**). This phenomenon facilitates a favorable alignment between the BCC and B2 phases. In the course of the B19' phase transition (stage III, ε=2.6%-8.6%), the *d*-spacing strain of the BCC phase increases (**Figure 4b**). The slope during this stage is higher than that in the plastic regime (stage IV, ε>8.6%), indicating the presence of lattice strain and

dislocation slip in the BCC phase. Notably, this alignment between the BCC phase and the B19' phase is achieved primarily through lattice strain rather than dislocation slip, a principle well-documented in studies involving nanowire and shape memory alloy composites, known as the lattice strain matching approach[1,36]. The lattice strain matching approach considerably diminishes the intensity of the elastic strain field at the phase boundary. As we enter stage IV (ε>8.6%), the *d*-spacing strain of the BCC phase gradually increases, with the corresponding slope being lower than that in stage III (ε=2.6%-8.6%). This suggests that the BCC phase now predominantly undergoes dislocation slip. The B19' phase transition primarily occurs in stage III (ε=2.6%-8.6%) (**Figure 4c**). The fraction of the B19' phase exhibits a rapid increase with macro-strain, with approximately 75% of the B2 phase ultimately transforming to the B19' phase by the end of this stage. In the early period of stage IV (ε=8.6%-16.7%), the fraction of the B19' phase remains relatively constant, possibly owing to the orientation of the B2 phase, which does not favor martensitic phase transformation. However, in the later period (ε>16.7%), the residual B2 phase initiates transformation into the B19' phase, suggesting that increased stress and strain trigger the reinitiation of martensitic phase transformation.

Figure 4d presents the *in-situ* synchrotron XRD measurement under cyclic loading, revealing a distinct reversible B2⇌R⇌B19' transition. In the initial loading-unloading cycle (O-A-B, ε=0-3%), the BCC phase peak position shifts leftward during loading (O-A) and then rightward during unloading (A-B). Initially, the peak width remains constant until significant broadening close to point A, indicating elastic deformation in the BCC phase, followed by plastic deformation beyond its elastic limit, generating dislocations and peak broadening. The B2 phase transforms to the R phase during loading (O-A) and reverses to the B2 phase during unloading (A-B). The second cycle (B-C-D, ε=1.7%-6.7%) sees the BCC phase peak position shift leftward during loading (B-C) and rightward during unloading (C-D). Peak width remains initially constant, gradually broadening during loading (indicating elastic and plastic deformation) and remaining constant during unloading. The B2→R→B19' phase

transition occurs during loading (B-C), with the reverse transition during unloading (C-D). In the third cycle (D-E-F, ε=4.2%-18%), the BCC phase undergoes elastic and plastic deformation during loading (D-E) and primarily elastic deformation during unloading (E-F). Similar to the previous cycle, the B2→R→B19' phase transition occurs during loading (D-E), with the reversed transition during unloading (E-F). After unloading, the residual B19' phase remains (point F), primarily due to plastic deformation of the BCC phase hindering the B19' phase's reverse transformation. **Figure 4e** depicts *d*-spacing strain versus macro-strain for the BCC and B2 phases during cyclic loading. Residual stress persists in both phases post-unloading. A negative *d*-spacing strain reflects tensile stress, whereas a positive value indicates compressive stress. Specifically, after unloading at different stages, we find that the BCC phase exhibits *d*-spacing strains of -0.037% (at point B), -0.131% (at point D), and -0.199% (at point F), respectively. In contrast, the B2 phase displays *d*-spacing strains of 0.035% (at point B), 0.059% (at point D), and 0.093% (at point F), respectively. These observations imply that tensile stress persists in the BCC phase after unloading, while the B2 phase maintains compressive stress. With an increasing number of cycles, residual stress becomes more pronounced. In the BCC phase, tensile stress partially counteracts the applied compressive stress during subsequent loading, enhancing the elastic strain limit, reaching 3.2% during the third unloading. Furthermore, for reversible phase transformations, the B2≒R transformation primarily occurs at low strain (< 6.7%), while the B2≒B19' transformation mainly takes place at high strain (> 6.7%) (**Figure 4f**). Plastic deformation induced by the BCC phase at elevated strain levels impedes the B19'→R→B2 phase transition during unloading, resulting in a substantial 60% residual presence of B19' post-unloading.

Discussion

We present a schematic representation of the deformation mechanisms in $Ni_{40}Ti_{40}(NbMoTaW)_{20}$ during continuous and cyclic loading processes (**Figure 4g**). During the loading process, in stage I (ε=0%-1.8%), the material undergoes the B2→R

transformation within the B2 phase, concurrently experiencing elastic strain in both the untransformed B2 and BCC phases. In stage II (ε=1.8%-2.6%), R→B19' and B2→B19' transitions take place. The untransformed B2 and BCC phases continue their elastic deformation. Progressing to stage III (ε=2.6%-8.6%), the B19' phase fraction increases with strain, with the B19' phase initially undergoing elastic deformation, followed by plastic deformation. The BCC phase and the residual B2 phase undergo plastic deformation during this stage. In stage IV (ε=8.6%-16.7%), plastic deformation occurs in both the B19' and BCC phases, culminating in the transformation of the residual B2 phase into the B19' phase. During unloading, the B19'→B2 transformation takes place. After unloading, the BCC phase experiences microscopic tensile stress, while the B2 phase incurs microscopic compressive stress. Therefore, in $Ni_{40}Ti_{40}(NbMoTaW)_{20}$ composite, the B2 NiTi matrix seamlessly integrates with the BCC phase, ensuring exceptional mechanical performance and recoverable strain capacity.

We harness the HEA concept to craft an inventive $Ni_{40}Ti_{40}(NbMoTaW)_{20}$ composite, uniting exceptional strength, ductility, and recoverable strain. Refractory HEAs inherently feature elevated intrinsic strength and pronounced lattice distortion[19,37,38], both pivotal in achieving the high strength observed in the $Ni_{40}Ti_{40}(NbMoTaW)_{20}$ composite. Additionally, within our $Ni_{40}Ti_{40}(NbMoTaW)_{20}$ composite, the BCC phase exhibits a high ideal configurational entropy (**Supplementary Table 1**). The high configurational entropy fosters the formation of a stable BCC solid solution phase[39], eliminating competing intermetallic compounds within the composite matrix. Thus, in $Ni_{40}Ti_{40}(NbMoTaW)_{20}$, the fraction of the brittle Ti_2Ni phase is minimized. This reduction significantly enhances the ductility of the $Ni_{40}Ti_{40}(NbMoTaW)_{20}$ composite (**Figure 1a**). Furthermore, during loading, the BCC phase exhibits a substantial elastic strain of 2.7% (**Figure 4b**), attributed to the effect of lattice strain matching between the transformation lattice distortion of the B2 NiTi matrix and the elastic strain of the BCC phase[40]. These unique micromechanical characteristics further underpin the high strength and large ductility of $Ni_{40}Ti_{40}(NbMoTaW)_{20}$. Moreover, multiple-element doping induces a multi-step phase

transition process in $Ni_{40}Ti_{40}(NbMoTaW)_{20}$ composite, prompting the occurrence of the B2→R→B19' phase transition during continuous loading and the B2⇌R⇌B19' phase transition during cyclic loading. Consequently, the combination of lattice strain matching and the reversible B2⇌R⇌B19' phase transition plays a pivotal role in imparting $Ni_{40}Ti_{40}(NbMoTaW)_{20}$ with its remarkable ductility and substantial recoverable strain. Importantly, the extensive compositional flexibility of HEAs, coupled with the manifold advantages stemming from the aforementioned structural features, markedly expands the design landscape for NiTi-based composites. This boundless potential facilitates the development of innovative NiTi-based composites that seamlessly integrate a range of exceptional properties into a unified whole.

In summary, we pioneer the utilization of the HEA concept in the fabrication of NiTi-based composites. The developed composite is primarily composed of a B2 NiTi matrix and a BCC compositionally complex phase. Importantly, the composite exhibits remarkable attributes, featuring exceptional strength, large ductility, and a superb recoverable strain capacity. Notably, it showcases a compressive strength of 3274 MPa, a fracture strain of 44.2%, and a recoverable strain of 7.3%, surpassing the overall performance of the majority of NiTi-based composites. The extraordinary mechanical performance is attributed to the unique structural characteristics of the compositionally complex phase and the lattice strain matching induced by phase transitions. Furthermore, multi-element microalloying within the B2 phase introduces a reversible B2⇌R⇌B19' phase transition process, resulting in a significant recoverable strain. This work not only introduces a novel category of NiTi-based composites but also offers valuable insights into strategies for enhancing their performance through the HEA concept.

Methods

Material preparation. Alloy ingots with a nominal composition of $Ni_{40}Ti_{40}(NbMoTaW)_{20}$ (at.%) were prepared by arc melting a mixture of pure metals (purity, >99.9 weight%) in a Ti-gettered high-purity argon atmosphere. The ingots were remelted at least eight times to ensure chemical homogeneity, and then drop-cast into a water-cooled copper mold with a dimension of 10×10×60 mm^3.

Mechanical measurements. Compression and cyclic compression tests were conducted at room temperature using an electric universal material testing machine (AGS-X-50KN) with a loading/unloading rate of 1×10^{-3} s^{-1}. The sample size is Φ4 mm × 6 mm. At least five samples were tested. In the loading-unloading tests, cyclic compression strains increased in 3% increments, starting at 3%, and continued until reaching failure.

Microstructural characterization. Microstructure and morphology were characterized by MIRA3 LMU scanning electron microscope (SEM, TESCAN company) operating at 20 kV. The energy-dispersive X-ray spectroscopy (EDS) was utilized to analyze the elemental distribution. The area fraction of each phase was calculated and measured by ImageJ software. The SEM sample was initially polished with 2000-grit SiC paper. Then, the sample was mechanically polished with a diamond plaster in a metallographic polishing machine (LMD-2C). Subsequently, the sample was polished with a colloidal silica suspension in a vibratory polishing machine (Vibra 304). Transmission electron microscopy (TEM, FEI Talos F200X) operating at 200 kV. The TEM sample was mechanically ground to a thickness of 50 μm and then twin-jet electropolished using 10 % sulfuric acid + 90 % methanol (vol.%) solution under a temperature of -20 °C, a voltage of 15 V. Phase transformation behavior of the composite was studied through differential scanning calorimetry (DSC) using a TA DSC25 unit at a cooling/heating rate of 10 K/min in a nitrogen atmosphere.

***In-situ* synchrotron high-energy X-ray diffraction.** *In-situ* high-energy X-ray

diffraction (XRD) during compression was carried out at the beamline P07-HEMS of PETRA III, Deutsches Elektronen-Synchrotron (DESY)[41]. Uniaxial compression was performed at room temperature (RT) using a modified dilatometer Bähr 805A/D equipped with a deformation unit[42]. Sequences of entire Debye-Scherrer rings were recorded from the bulk material in transmission mode using a Perkin Elmer XRD 1621 image-plate detector. The incident X-ray beam (perpendicular to the loading direction) was positioned at the center of the sample's length. A slit size of 0.8 × 0.8 mm^2 resulting in a gage volume of 0.8 × 0.8 × 4 mm^3 was used. The sample-detector distance and acquisition time were 1600 mm and 1 s, respectively. An illustrative diagram of the experimental setup is presented in ref.[43]. The beam energy was 100 keV (wavelength = 0.124 Å). The instrument parameters were calibrated using a LaB6 powder standard. One-dimensional (1-D) high-energy XRD patterns were obtained by integrating across all angles in the 2-D diffraction patterns under various applied strains. The lattice strain under various applied strains was fitted by distorting two-dimensional (2-D) diffraction patterns using GSAS-II software package[44]. Positive for compression and negative for tension in the direction of loading.

Acknowledgments

This research was funded by the National Natural Science Foundation of China (Nos. 52371153, 52101194), the Natural Science Foundation of Hunan Province (No. 2022JJ40078), The Fundamental Research Funds for the Central Universities (Nos. 531118010621, 531118010671) and The Science and Technology Innovation Program of Hunan Province (No. 2022RC1083). The authors would like to acknowledge the support provided by A. Stark and N. Schell (Helmholtz-Zentrum Hereon) for the diffraction experiments performed at the P07-HEMS beamline. The Deutsches Elektronen-Synchrotron (DESY) is acknowledged for the provision of synchrotron radiation facilities in the framework of the proposal I-20221372 EC. P.B.V. acknowledges financial support from the Spanish Ministry of Science through the Ramón y Cajal grant RYC2020-029585-I.

Author contributions

Y.Z.S., Z.F.L., and Z.P.L. supervised and conceived this project. J.Y.G. fabricated the materials and characterized the mechanical properties, phase transition behavior, and microstructure of the materials. P.B.V. and Y.M. conducted the in-situ high-energy X-ray diffraction experiments. Y.H.C. conducted the DSC experiments. C.M. and M.J.Y. conducted and analyzed TEM experiments. Y.T. and J.Z.H. conducted the cyclic compression experiments. J.Y.G., Y.Z.S., Z.F.L., and Z.P.L. wrote the manuscript. All authors discussed the results and commented on the manuscript.

Competing interests

The authors declare no competing interests.

Additional information

Supplementary information The online version contains supplementary material available at xxx.

Correspondence and requests for materials should be addressed to Yunzhu Shi, Zhifeng Lei or Zhaoping Lu.

Data availability

The datasets generated and/or analyzed during the current study are available from the corresponding authors on request.

References

[1] S. Hao et al., Science 339 (2013) 1191–1194.

[2] E. Farber et al., Mater. Today Proc. 30 (2020) 761–767.

[3] J. Mohd Jani et al., Mater. Des. 1980-2015 56 (2014) 1078–1113.

[4] S.K. Patel et al., Mater. Today Proc. 33 (2020) 5548–5551.

[5] J. Zhang et al., Sci. Rep. 5 (2015) 8357.

[6] K. Otsuka, X. Ren, Prog. Mater. Sci. 50 (2005) 511–678.

[7] F. Guo et al., J. Alloys Compd. 781 (2019) 1–7.

[8] X. Yao et al., Mater. Today Commun. 29 (2021) 102779.

[9] J. Jiang et al., Mater. Sci. Eng. A 633 (2015) 121–124.

[10] D. Jiang et al., Scr. Mater. 78–79 (2014) 53–56.

[11] Y. Li et al., Mater. Sci. Eng. A 866 (2023) 144672.

[12] B. Cantor et al., Mater. Sci. Eng. A 375–377 (2004) 213–218.

[13] J.-W. Yeh et al., Adv. Eng. Mater. 6 (2004) 299–303.

[14] E.P. George, D. Raabe, R.O. Ritchie, Nat. Rev. Mater. 4 (2019) 515–534.

[15] Z. Lei et al., Sci. Adv. 6 (2020) eaba7802.

[16] C. Lee et al., Acta Mater. 160 (2018) 158–172.

[17] D.B. Miracle, O.N. Senkov, Acta Mater. 122 (2017) 448–511.

[18] Y.F. Ye et al., Mater. Today 19 (2016) 349–362.

[19] C. Lee et al., Adv. Mater. 32 (2020) 2004029.

[20] Q.F. He et al., Nature 602 (2022) 251–257.

[21] Z. Lei et al., Nature 563 (2018) 546–550.

[22] Q. Ding et al., Nature 574 (2019) 223–227.

[23] X. Chen et al., Nature 592 (2021) 712–716.

[24] R. Zhang et al., Nature 581 (2020) 283–287.

[25] L. Wang et al., Nat. Mater. 22 (2023) 950–957.

[26] S. Chen et al., Nat. Commun. 12 (2021) 4953.

[27] Y. Chen et al., Acta Mater. 180 (2019) 243–259.

[28] S. Liu et al., Mater. Sci. Eng. A 801 (2021) 140434.

[29] C. Bewerse, L.C. Brinson, D.C. Dunand, Mater. Sci. Eng. A 627 (2015) 360–368.

[30] J.W. Yeh et al., Mater. Sci. Forum 560 (2007) 1–9.

[31] H. Shi et al., Acta Mater. 74 (2014) 85–95.

[32] X.B. Wang, B. Verlinden, J. Van Humbeeck, Mater. Sci. Technol. 30 (2014) 1517–1529.

[33] S. Miyazaki, S. Kimura, K. Otsuka, Philos. Mag. A 57 (1988) 467–478.

[34] B. Li, Y. Shen, Q. An, Acta Mater. 199 (2020) 240–252.

[35] D. Wang et al., Acta Mater. 58 (2010) 6206–6215.

[36] D.D. Johnson et al., Phys. Rev. Lett. 130 (2023) 166101.

[37] Y. Zou, H. Ma, R. Spolenak, Nat. Commun. 6 (2015) 7748.

[38] F. Wang et al., Science 370 (2020) 95–101.

[39] O.N. Senkov et al., J. Mater. Res. 33 (2018) 3092–3128.

[40] J. Zhang et al., Adv. Mater. 32 (2020) 1904387.

[41] P. Staron et al., Adv. Eng. Mater. 13 (2011) 658–663.

[42] N. Schell et al., Mater. Sci. Forum 772 (2013) 57–61.

[43] P. Barriobero-Vila et al., Mater. Sci. Eng. A 717 (2018) 134–143.

[44] B.H. Toby, R.B. Von Dreele, J. Appl. Crystallogr. 46 (2013) 544–549.

[45] Y. Wen et al., Acta Metall. Sin. Engl. Lett. 35 (2022) 317–325.

[46] W. Guo, H. Kato, Mater. Lett. 158 (2015) 1–4.

[47] S.H. Mills et al., Shape Mem. Superelasticity 6 (2020) 311–322.

[48] E. Wang et al., J. Alloys Compd. 775 (2019) 1307–1315.

[49] Y. Zhang et al., Acta Mater. 239 (2022) 118295.

[50] S. Wisutmethangoon, N. Denmud, L. Sikong, Mater. Sci. Eng. A 515 (2009) 93–97.

[51] Y.-H. Li, L.-J. Rong, Y.-Y. Li, J. Alloys Compd. (2002).

[52] Y. Qiu, M.L. Young, X. Nie, Shape Mem. Superelasticity 1 (2015) 310–318.

[53] P. Hua et al., Nat. Nanotechnol. 16 (2021) 409–413.

[54] S. Xiaoyun, L. Yan, Z. Fei, L. Shusuo, Chin. J. Aeronaut. 23 (2010) 715–719.

[55] A.J. Neurohr, D.C. Dunand, Acta Biomater. 7 (2011) 1862–1872.

[56] M. Morakabati et al., J. Alloys Compd. 499 (2010) 57–62.

[57] R. Xi et al., Virtual Phys. Prototyp. 18 (2023) e2126376.

[58] Y. Koizumi, Y. Ro, S. Nakazawa, H. Harada, Mater. Sci. Eng. A 223 (1997) 36–41.

[59] M. Zhang et al., Sci. Adv. 6 (2020) eaba5581.

[60] F. Guo et al., Metals 12 (2022) 620.

[61] J. Zhang et al., Appl. Phys. Lett. 105 (2014) 041910.

[62] S. Parvizi et al., Prog. Mater. Sci. 117 (2021) 100739.

[63] H. Kato, S. Fukushima, K. Sasaki, Adv. Struct. Mater. 73 (2017) 43-50.

[64] N. Shayesteh Moghaddam et al., Sci. Rep. 9 (2019) 41.

[65] X. Hu et al., J. Alloys Compd. 853 (2021) 157309.

[66] O. Benafan et al., Shape Mem. Superelasticity 2 (2016) 337–346.

[67] Q. Yang et al., Mater. Sci. Eng. -Struct. Mater. Prop. Microstruct. Process. 787 (2020).

[68] J. Zhang et al., Acta Mater. 130 (2017) 297–309.

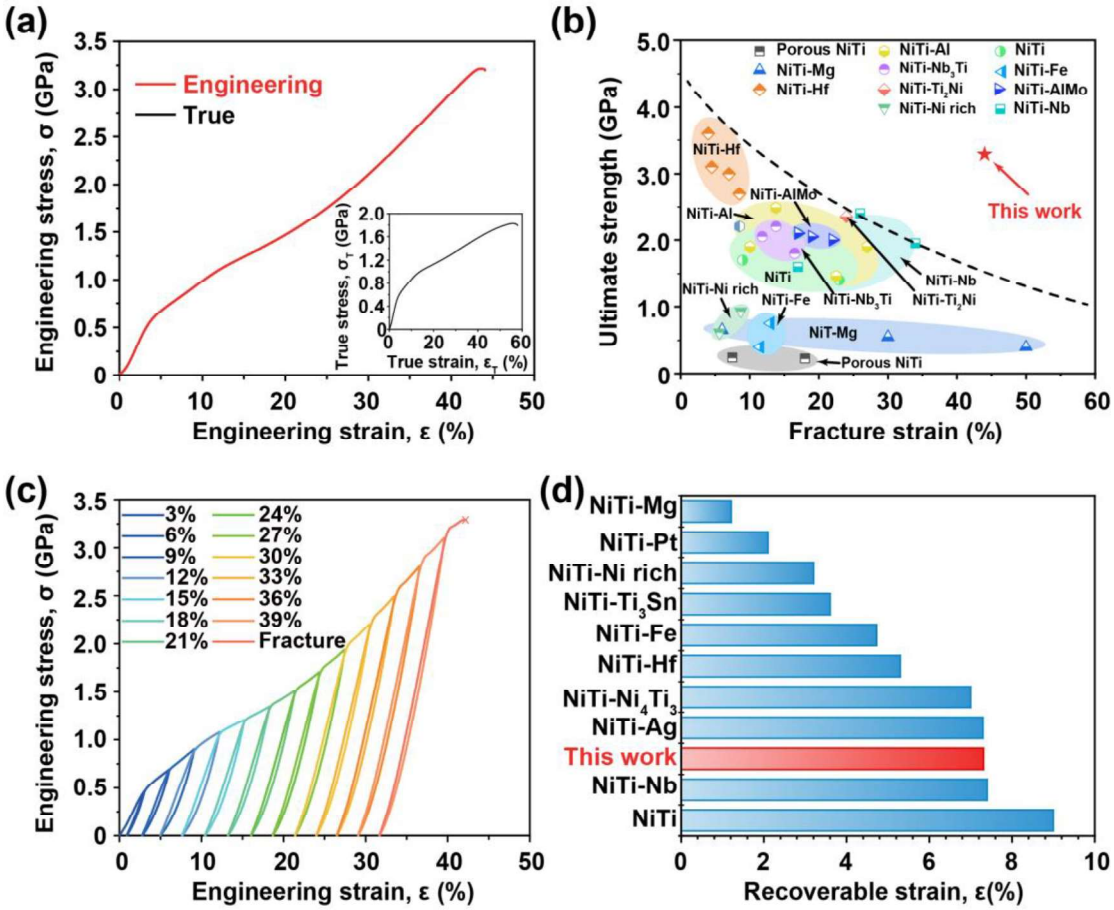

Figure 1. Mechanical and superelastic properties. (a) Compressive engineering stress-strain curve of the $Ni_{40}Ti_{40}(NbMoTaW)_{20}$ composite, with the inset displaying the corresponding true stress-strain curve. **(b)** Ultimate strength versus fracture strain of the $Ni_{40}Ti_{40}(NbMoTaW)_{20}$ composite in comparison with NiTi and other NiTi-based composites[11,45–62]. **(c)** Engineering stress-strain curve during cyclic compression for the $Ni_{40}Ti_{40}(NbMoTaW)_{20}$ composite. During the loading-unloading test, the cyclic compression strains range from 3%, 6%, 9%, 12%, and so forth until failure occurs. **(d)** Recoverable strain of the $Ni_{40}Ti_{40}(NbMoTaW)_{20}$ composite in comparison with NiTi and other NiTi-based composites[1,29,45,47,52,53,56,59–68].

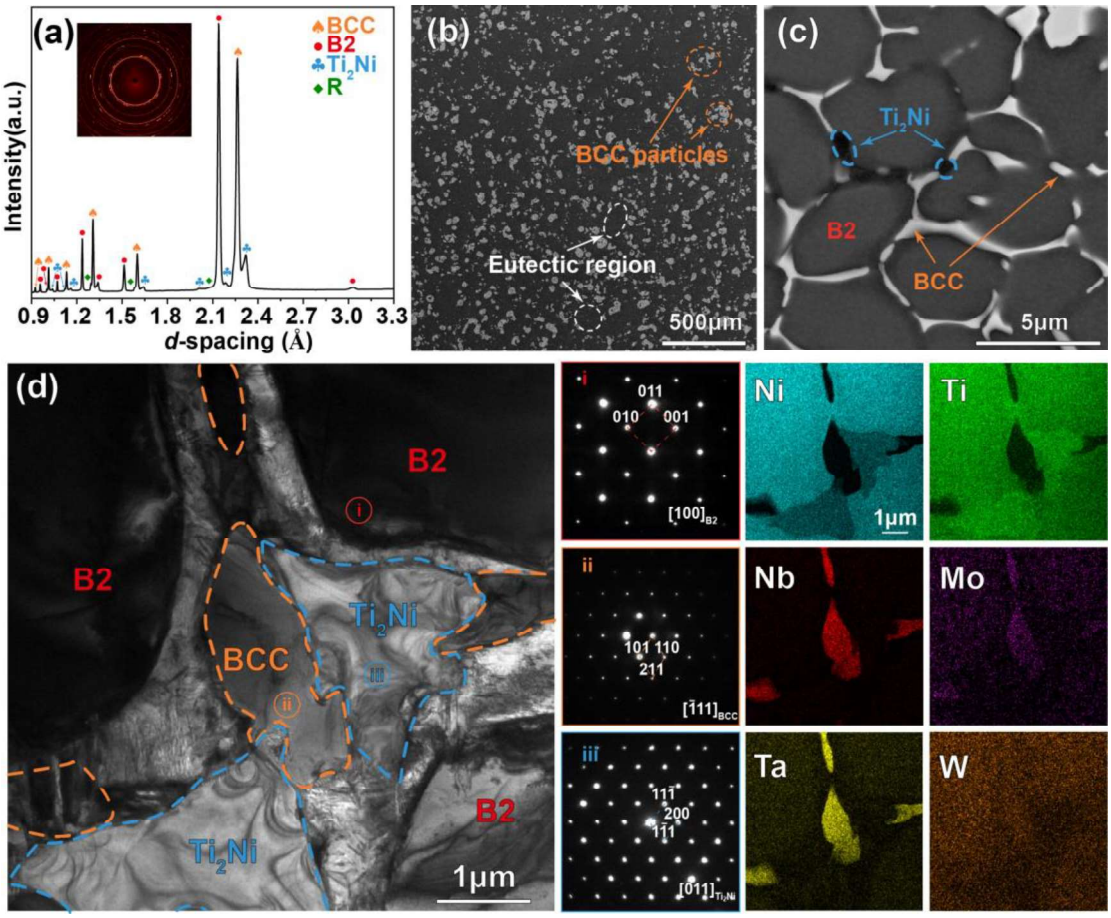

Figure 2. Microstructure characterization. (a) Synchrotron high-energy X-ray diffraction (XRD) pattern of the $Ni_{40}Ti_{40}(NbMoTaW)_{20}$ composite, with the inset revealing the Debye–Scherrer rings. **(b)** Scanning electron microscope (SEM) image of the $Ni_{40}Ti_{40}(NbMoTaW)_{20}$ composite. **(c)** Corresponding local enlargement of (b). The white arrows highlight the eutectic region, the orange arrows depict the body-centered cubic (BCC) particles and strips, and the blue arrows illustrate the Ti_2Ni strips. **(d)** Bright-field transmission electron microscopy (TEM) image offering a detailed view of the B2 NiTi matrix, BCC phases, and the Ti_2Ni precipitates. **(i), (ii)** and **(iii)** are the corresponding selected area electron diffraction pattern of the B2 NiTi, BCC and Ti_2Ni phases. The two columns on the right showcase the elemental distribution mapping, illustrating the spatial distribution of Ni, Ti, Nb, Mo, Ta, and W.

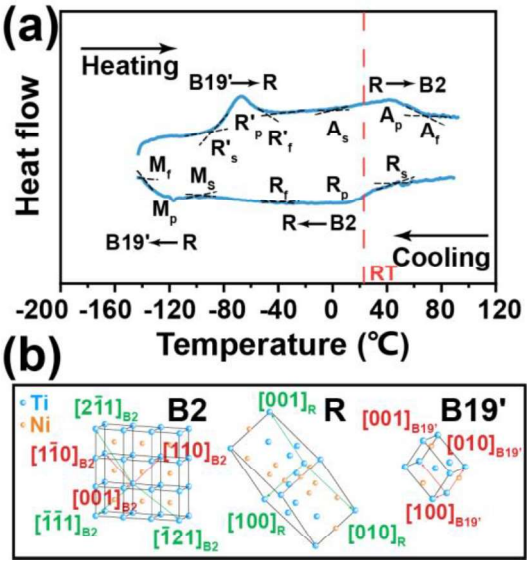

507

508 **Figure 3. Transformation behavior. (a)** Differential scanning calorimetry (DSC)
509 curve for the $Ni_{40}Ti_{40}(NbMoTaW)_{20}$ composite, providing insights into various
510 transformation temperatures. Key points on the DSC curve are labeled as follows: RT
511 (room temperature), R_s (start temperature of B2→R transition), R_p (peak temperature
512 of B2→R transition), R_f (finish temperature of B2→R transition), M_s (start temperature
513 of R→B19' martensitic transformation), M_p (peak temperature of R→B19' martensitic
514 transformation), M_f (finish temperature of R→B19' martensitic transformation), R'_s
515 (start temperature of B19'→R transition), R'_p (peak temperature of B19'→R transition),
516 R'_f (finish temperature of B19'→R transition), A_s (start temperature of R→B2 austenitic
517 transformation), A_p (peak temperature of R→B2 austenitic transformation), and A_f
518 (finish temperature of R→B2 austenitic transformation). **(b)** Schematic diagram
519 illustrating the interconversion between the B2, R, and B19' phases.

520

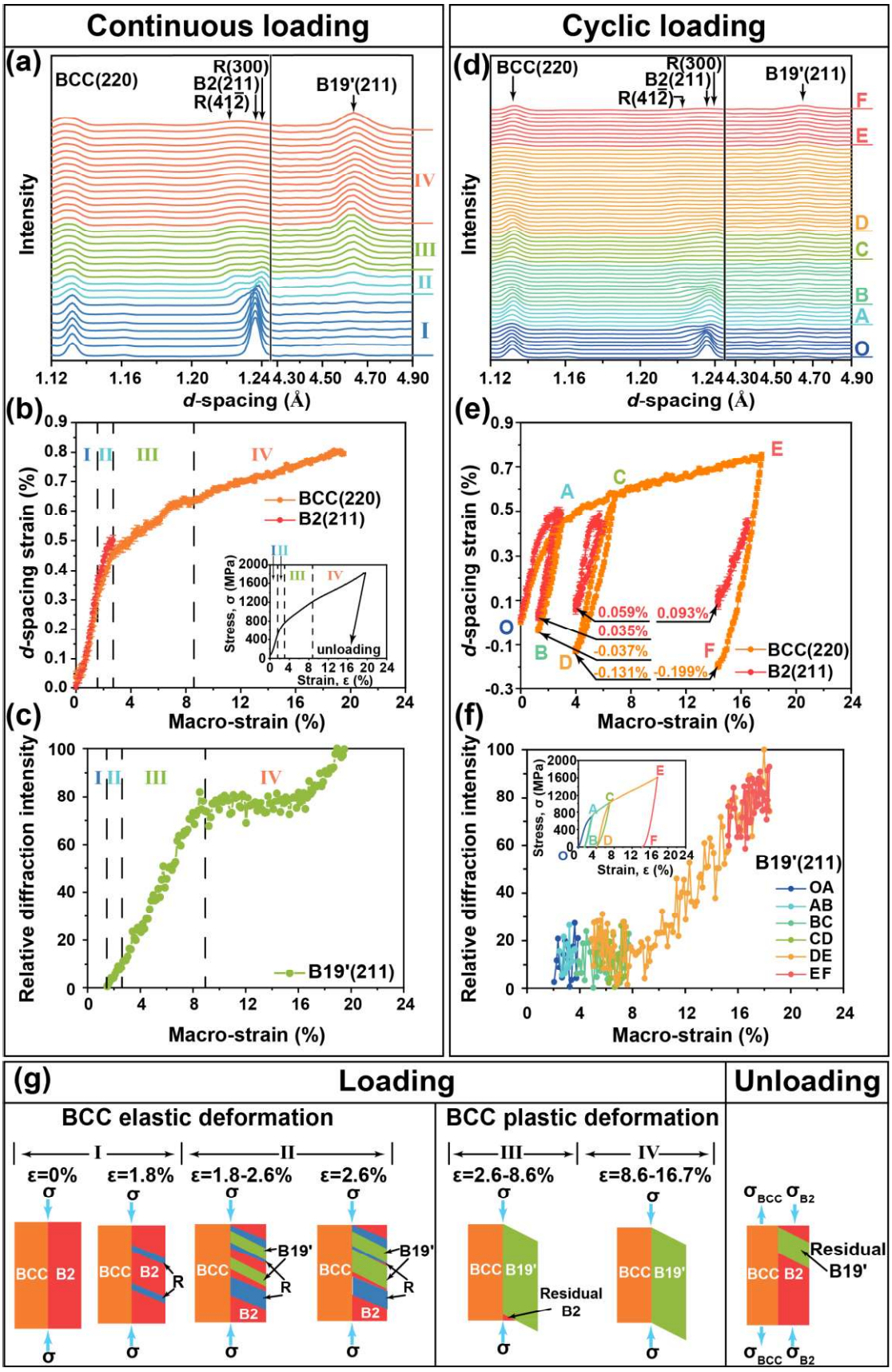

Figure 4. Deformation mechanisms. (a) *In-situ* synchrotron high-energy X-ray

diffraction patterns captured during continuous loading, revealing the dynamic evolution of peaks corresponding to BCC (220), B2 (211), R ($41\bar{2}$), R (300), and B19' (001). **(b)** The progression of *d*-spacing strain for BCC (220) and B2 (211) planes during continuous loading, with analysis data obtained parallel to the loading direction. An inset provides a schematic illustration of the continuous loading process. **(c)** The evolution of the relative diffraction intensity of B19' (001) peaks during continuous loading. **(d)** *In-situ* synchrotron high-energy X-ray diffraction patterns recorded during cyclic loading. **(e)** The evolution of *d*-spacing strain for BCC (220) and B2 (211) planes during cyclic loading, with analysis data acquired parallel to the loading direction. **(f)** The evolution of the relative diffraction intensity of B19' (001) peaks during cyclic loading. An inset offers a schematic depiction of the cyclic loading process. **(g)** A schematic representation elucidating the elastic-plastic deformation within the BCC phase and the phase transition in the B2 matrix. Here, σ represents the external stress; σ_{BCC} symbolizes the microscopic stress on the BCC phase after unloading, and σ_{B2} denotes the microscopic stress on the B2 matrix after unloading.